

Preparation and Characterization of New Modified System: Polyaniline/1.5-Naphtalene Disulfonic Acid as Novel Photocatalyst in the H₂ Production

F. Z. Hamlaoui

USTHB

N. Naar

USTHB

Faouzi Saib (✉ saib.dz@gmail.com)

USTHB <https://orcid.org/0000-0001-8259-5738>

M. Trari

USTHB

Research Article

Keywords: PANI-NDSA, semiconductor, photo-electrochemical, electrochemical impedance spectroscopy, hydrogen, visible light

Posted Date: March 22nd, 2021

DOI: <https://doi.org/10.21203/rs.3.rs-329171/v1>

License:   This work is licensed under a Creative Commons Attribution 4.0 International License.

[Read Full License](#)

Preparation and Characterization of New Modified System: Polyaniline/1.5-Naphtalene Disulfonic Acid as Novel Photocatalyst in the H₂ Production

F. Z. Hamlaoui ^a, N. Naar ^a, F. Saib^{1, b, c}, and M. Trari ^c

^a *Laboratory of Macromolecular Synthesis and Thio-Organic Macromolecular, Faculty of Chemistry, USTHB, BP 32, 16111 Algiers, Algeria*

^{b, 1} *Centre de Recherche Scientifique et Technique en Analyses Physico-Chimiques (CRAPC), BP384, Bou-Ismaïl, RP 42004, Tipaza, Algeria*

^c *Laboratory of Storage and Valorization of Renewable Energies, Faculty of Chemistry, USTHB, BP 32, 16111 Algiers, Algeria*

Abstract

The semiconducting properties of the system Polyaniline / 1.5-naphtalene disulfonic acid are investigated for the first time to assess its photocatalytic performance for the hydrogen evolution under visible light irradiation. PANI is thermally stable up to ~ 300 °C, above which a weight loss of ~ 1.2% occurs. The X-ray diffraction pattern shows broad peaks with a particle size of ~ 7 nm, leading to an active surface area of ~ 400 m² g⁻¹. A direct optical transition at 1.96 eV, is determined from the diffuse reflectance spectrum. The electrical conductivity of PANI-NDSA follows an exponential law with activation energy of 0.24 eV. The *p*-type conduction of PANI-NDSA is evidenced from the (capacitance⁻² – potential) characteristic plot; a flat band potential (E_{fb}) of 0.82 V_{SCE} and a holes density (N_A) of 8.43×10^{24} m⁻³ are determined in neutral solution (Na₂SO₄ 0.1 M). The electrochemical impedance spectroscopy, measured over an extended frequency domain (1 mHz - 10¹⁰ Hz), indicates the contribution of both the bulk and grain boundaries with a constant phase element (CPE). As application, PANI-NDSA is successfully tested for the hydrogen production upon visible light owing to the potential of its conduction band (-0.75 V_{SCE}), less cathodic than that of H₂O/H₂ (~ -0.30 V_{SCE}). H₂ liberation rate of 3840 h⁻¹ (g catalyst)⁻¹ and a quantum efficiency of 0.34% under full light (29 mW cm⁻²) are obtained using Fe(CN)₆⁴⁻ as reducing agent. The photoactivity is completely restored during the second cycle.

Keywords: PANI-NDSA; semiconductor; photo-electrochemical; electrochemical impedance spectroscopy; hydrogen; visible light.

¹ Corresponding author

E-mail address: saib.dz@gmail.com (F. SAIB) ; solarchemistry@gmail.com (M. TRARI)

Introduction

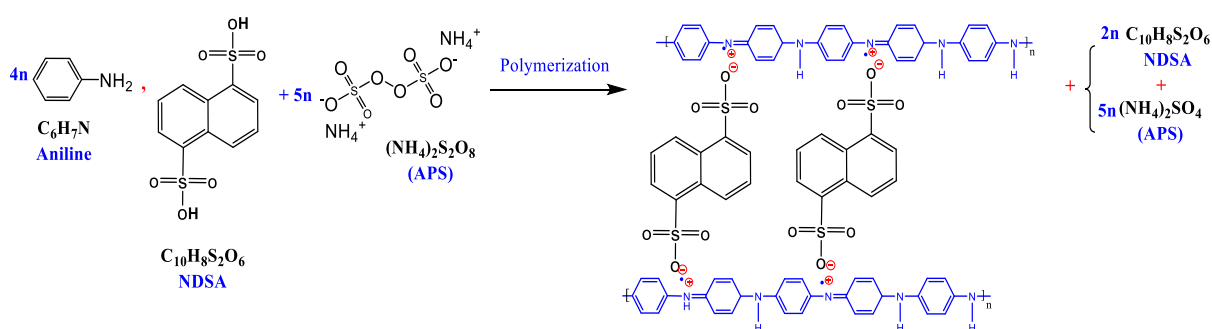
Fossil energy resources start to run out and the solar energy can partially take over. It becomes more and more attractive and meets an increasing demand in many fields like the photovoltaic [1,2] thermal conversion [3,4] photocatalysis [5,6] and environmental protection [7–9]. With a mean insolation of 1200 W m^{-2} and a duration exceeding 3000 h year^{-1} (South Algeria), the sun is an inexhaustible energetic source that represents a promising alternative. However, the intermittency of this energy requires long-term storage and appropriate strategies are developed in this direction. In this regard, hydrogen is a clean fuel with no emission of the greenhouse gas CO_2 , the first responsible of the global warming [10,11]. Accordingly, it remains attractive for the chemical storage [12–14] with a high energy density per unit volume; it can be stored during the off hours and produced on demand. It can also be used in fuel cells that convert the mixture (H_2/O_2) into electricity more efficiently and cleanly than in combustion engines.

The water splitting into hydrogen and oxygen can occur thermally [15–17], by thermochemical cycles [18,19], steam reforming [20], zinc acid [21–23], aluminium upon treatment with bases and by photocatalysis [24,25]. In the first case, only a small amount of water gas can be decomposed at high temperature ($> 2200 \text{ }^\circ\text{C}$) using solar concentrators. Additionally, the separation of gases (O_2 and H_2) renders the process complex and the gases mixture must be quenched to prevent their recombination. By contrast, the water photo-splitting occurs under soft conditions with no special equipment. However, the semiconductor (SC) oxides like SnO_2 [26,27], NaNbO_3 [28,29] and TiO_2 used in photocatalysis [30,31], are stable against photo-corrosion but have a large forbidden band ($E_g > 3 \text{ eV}$) and are consequently less attractive for the solar energy conversion where less than 5% of UV light accounts for the solar radiation [32,33]. Therefore, some recent studies were directed toward organic semiconductors (SCs) [34,35]. In this respect, the conducting polymers [36] start to arouse a growing interest from an academic point of view [37–41]. Such materials not only work in a similar way to mineral semiconductors but also have positive features such as environmental friendliness characteristics, easy preparation and light weight. Using a polymer as photoelectrode is original and modified PANI is attractive owing to its better stability and low cost [42,43]. The potential of the conduction band (CB) is more cathodic than the H_2 level making PANI attractive for the reduction of water into hydrogen [44,45]. It has a small band gap (E_g) allowing the exploitation of a large part of sunlight [46]. Unlike physical characterization, the photo-electrochemical (PEC) properties of modified PANI and hydrogen evolution have been little studied. Conducting PANI is sensitive to the pH and the chain of polyaniline undergoes a deprotonation

in basic solution (pH ~ 9 - 11). Conversely, in acid medium (pH ~ 2 - 4) it converts into insulator quinoid accompanied by the deintercalation of counter anions where the chain becomes protonated with a small increase of the conductivity. The present work is devoted to the PEC characterization of the modified polyaniline/1.5-naphtalene disulfonic acid (PANI-NDSA) prepared by oxidation of aniline using persulfate as oxidant and 1.5-naphtalene disulfonic acid (NDSA) as dopant. The photo-electrochemical characterization, reported for the first time, is a preamble of the application for the hydrogen formation under visible light illumination.

2. Experimental

PANI-NDSA was synthesized by interfacial chemical oxidation of aniline using $(\text{NH}_4)_2\text{S}_2\text{O}_8$ as oxidant and 1.5-naphtalene disulfonic acid (NDSA) as dopant, with molar ratio NDSA/aniline of 1.5 and oxidant/aniline of ~ 1. First, in a three-necked flask containing 3 mL of aniline dissolved in 30 mL of CHCl_3 . Then, we added 1.5g of NDSA and 3.67g of $(\text{NH}_4)_2\text{S}_2\text{O}_8$ dissolved in appropriate quantity of water; in an ice bath (0 °C) under stirring. To ensure a maximum doping, the green colored colloidal PANI solution was left overnight open to atmosphere. PANI-NDSA was washed with a mixture distilled water/ethanol, followed by successive washing with distilled water until the total elimination of acid traces. The final green powder was recovered by filtration and dried in an oven of 50°C for 48 h. The preparation process of PANI-NDSA is summarized in **Fig. 1**. The polymerization mechanism of PANI in the form of repeated linear "quinoid and benzoid" groups is proposed. It introduces intentionally holes by removing two electrons from alternate nitrogen atoms as can be seen in scheme 1.



Scheme. 1. Mechanism of PANI-NDSA doping polymerization.

During the interfacial polymerization of polyaniline, 1.5-Naphtalene Disulfonic Acid (NDSA, powder) was used as dopant. PANI is an intrinsically conductive polymer; insulator in the neutral state. Therefore, to modify the transport properties with an insulating-

semiconductor transition), a direct chemical dopant is required and NDSA is suitable in such a case. The latter is a stable diacid up to 290 °C, thus providing function-structure stability (scheme 1).

Thermal analysis (TG) was carried out using TGA Q 500 TA Instrument at a heating rate of 10 °C min⁻¹. The phases were identified by X-ray diffraction using Cu K α anticathode ($\lambda = 0.15418$ nm) at a scanning rate of 2° (2 θ) min⁻¹. The UV-Visible spectra were plotted with a spectrophotometer (Specord Plus 2000) attached to an integrating sphere, PTFE was used as standard. The electrical conductivity (σ) was measured in the interval (300–450 K) by the two probe method using home-made equipment. For the thermo-power, the pellet was sandwiched between two stainless steels; the thermal gradient (ΔT) was obtained by Cr-Al thermocouples whereas the electro-motive force (e.m.f.) was measured thanks to a LCR Agilent 4263 B LCR equipment.

The permittivity ($\epsilon \sim 5920$) of PANI-NDSA was determined from dielectric measurements at 10 kHz on dense pellet with a GW Instek GDM- 8261A LCR-meter.

The powder was compressed into discs ($\varnothing = 1.3$ cm, thickness 0.6 mm) under 5×10^2 MPa. To minimize the contact resistance, Ag paint was contacted to the back surface of the discs, which are enrobed in Teflon tubes leaving a contact surface area of 1.32 cm² with the electrolyte. The photoelectrochemical (PEC) characterization was done in aqueous solutions in potentiostatic mode using a standard Pyrex cell with a Pt emergency electrode. The potential of the working electrode was monitored by a computer controlled potentiostat (Solartron, SI: 1287) and given with respect to a saturated calomel electrode (SCE). The capacitance measurements are plotted at a frequency of 10 KHz. The point of charge zero (pzc) is measured from the equilibrium pH of an aqueous powder solution with a digital pH meter. The complex impedance spectroscopy (EIS) was undertaken with small amplitude wave signals in a wide region (10^{-2} - 10^5 Hz) [47–51].

The photocatalysis was done in a double walled Pyrex reactor connected to a cooling system, the temperature was regulated at 50 ± 1 °C; 125 mg of PANI-NDSA powder were dispersed in 250 mL of electrolytic solution Na₂SO₄ (10^{-2} M) containing K₄Fe(CN)₆ (10^{-3} M) under magnetic agitation (210 rpm). Prior each experiment, N₂ gas was bubbled in the solution for 20 min at a constant rate of 5 mL mL⁻¹. Visible light illumination was provided by three tungsten lamps (3 \times 200 W), giving a total intensity of 29 mW cm⁻² (2.09×10^{19} photons s⁻¹). The liberated gas was identified as hydrogen by gas chromatography (Shimadzu IGC 121 ML). The

volume was quantified with a water manometer in a graduated burette (5 mm inner diameter). Blank experiments were realized and no H₂ evolution was observed in the dark. The solutions were prepared from reagents grade chemicals in demineralized water.

Results and discussion

The TG plot of PANI-NDSA (**Fig. 2**) is carried out in order to delimit the thermal stability of PANI-NDSA. The decomposition, accounting for a first loss at ~ 50 ° C to 120 ° C attributed to the elimination of physisorbed water, a small weight loss (~ 1 %), occurs over a large temperature range; it starts at ~ 120°C and ends at ~ 290 °C with an inflexion point at ~300 °C. The XRD pattern illustrated in **Fig. 3** reveals the semi crystallinity of PANI with the characteristic peaks ($2\theta=15, 20$ and 25), in agreement with previous results [52–54]. The wide peaks with small crystallites, the size ($L \sim 7$ nm) is evaluated from the full width at half maximum $\{L= 0.94 \lambda(\beta \cos)^{-1}\}$. Assuming spherical crystallites, a minimal specific surface area of $410 \text{ m}^2 \text{ g}^{-1}$ is evaluated from the relation $\{S= 6 \times (\rho_{\text{exp}} L)^{-1}\}$, the experimental density ρ_{exp} ($= 1.03 \text{ g cm}^{-3}$) determined by picnometry.

The **Fig. 4** shows the FTIR spectrum of PANI doped with NDSA in the range (500-4000 cm^{-1}). The latter includes the existence of the absorption bands around 1566 and 1488 cm^{-1} are the characteristic bands of C=C quinoïd and benzoïd rings, respectively. The band around 3229 cm^{-1} is assigned to the N-H elongation. The bands at 1298 cm^{-1} and 1239 cm^{-1} are due to C-N stretch vibrations of the groups of benzoïd and quinoïd systems. The band located at 1121 cm^{-1} associated the vibration $\text{N}=\text{Q}^+=\text{N}$ of PANI-NDSA, confirms the delocalization and protonation of the polymer [55,56]. The existence of band at 801 and 872 cm^{-1} correspond to the deformation C-H of 1, 4 substituted phenyl and benzene rings, respectively. The peaks about 1029 cm^{-1} is attributed to C-N⁺ and SO₃⁻ confirming the doping, the peak at 702 cm^{-1} is assigned to S-O vibration corresponding to NDSA.

Optic and transport properties

The optical properties of PANI-NDSA, important in photocatalysis, are determined from the diffuse reflectance spectrum. The relation between the absorption coefficient (α , cm^{-1}) and the incident photon energy ($h\nu$, eV) is given by the Pankov relation:

$$(\alpha h\nu)^m = \text{Const} \times (h\nu - E_g) \quad (1)$$

The exponent m depends on the transition type, it is equal to 2 and 1/2 respectively for direct and indirect transitions. The extrapolation of the straight line $(\alpha hv)^2$ with the $h\nu$ -axis (**Fig. 5**) give a direct transition at 1.96 eV. The band structure of PANI-NDSA consists of a lowest unoccupied molecular orbital (LUMO) which constitutes the valence band (VB) separated by a forbidden band (E_g) from the highest occupied molecular orbital (HOMO: conduction band, CB), thus referring to $\pi \rightarrow \pi^*$ transition[36]. The conjugated poly-heterocycles have two states, not equivalent namely the aromatic and quinonic states. The transition from the aromatic to the quinonic state augments the energy of HOMO and decreases that of LUMO, which explains the narrowing of the gap at 1.03 eV[57].

The thermal dependence of the AC conductivity (σ) of PANI-NDSA shows a non degenerate behavior (**Fig. 6**) with a conduction mechanism by electrons jump among localized sites; an activation energy $E_a(= 0.24 \text{ eV})$ of was deduced from the slope $\log\sigma/dT$. The knowledge of the energetic position of the bands LUMO and HOMO is a prerequisite for the photocatalytic study and the photo-electrochemistry is widely used for providing the semiconducting properties. Such value indicates that the conduction mechanism occurs by small polaron hopping, behaving like a heavy particle with a limited free path and a low mobility at 300 K ($\mu_h= 8.78 \text{ cm}^2 \text{ V}^{-1} \text{ s}^{-1}$) as it could be anticipated from the moderate conductivity.

However, the thermo-power (S) defined as the proportionality constant between the gradients of potential (ΔV) and temperature (ΔT); is insensitive to defect states and grains boundaries and should highlight the conduction mechanism in PANI-NDSA. The positive sign of S over the studied temperature domain (**Fig. 7**), confirms that the majority charge carriers are holes, involved conduction mechanism by small polaron hopping among mixed states. S_{300K} averages 0.80 mV K^{-1} in agreement with a non-degenerate conductivity and should yield a density of $\sim 10^{18} \text{ cm}^{-3}$ where the lattice phonon scattering governs the conduction mechanism; in such a case S is expressed by:

$$S = \frac{k}{e} \left(\frac{5}{2} - A \right) \frac{E_s}{kT} \quad (2)$$

E_s (0.24 eV) is the thermal activation for the charge carriers and A an entropic constant which can be ignored for small polaron jump. The large difference between the energy values (E_σ and E_s) is an evidence of a conduction mechanism by small polarons in PANI-NDSA.

Photo-electrochemical characterization

PANI-NDSA is a potential photocatalyst for the energy supply and the photo-electrochemistry is a powerful tool to establish the energy band diagram (**Fig. 11**). The Intensity-Potential $J(E)$ plots were recorded to check the electrochemical stability and to elucidate the interfacial redox reactions; the measurements were carried out once the open circuit potential (*OCP*) stabilized. Na_2SO_4 (0.1 M) was used as support electrolyte because it has high conductivity.

The cyclic $J(E)$ characteristic of PANI-NDSA is plotted to elucidate the electrochemical behavior, the plot (**Fig. 8**) shows an hysteresis loop where the current is in conformity with a classical. Below ~ -0.30 V, the current shoots up due to H_2 liberation (gas bubbles were noticeable on the electrode) and the corresponding potential is found to be pH independent. One can mention in passage that the over-voltages are minimized and PANI-NDSA can be attractive in the water splitting.

The flat band potential (E_{fb}) of PANI-NDSA ($= +0.82$ V) is reliably provided from the intercept of the linear part to infinite capacity $C^{-2} = 0$ of the plot (**Fig. 9**):

$$C^{-2} = (2/e\epsilon\epsilon_0 N_A) \{V - V_{fb}\} \quad (3)$$

Where ϵ_0 is the permittivity of vacuum, e the electron charge and N_A the holes density. The permittivity ($\epsilon \sim 5920$) of PANI-NDSA was determined from dielectric measurements. The negative slope indicates semiconducting properties with p type behavior where holes are the majority carried; their density ($N_A = 8.43 \times 10^{18} \text{ cm}^{-3}$) was deduced from the slope dC^{-2}/dE with an enlarged space charge region:

$$W_o = \{2\epsilon\epsilon_0 (E - E_{fb})/e N_A\}^{1/2} \quad (4)$$

W_o (~ 2 nm) is obtained for an optimal band bending ($\Delta E = E_{fb} - E$) of 0.5 V and the measured capacity is principally due to SCR of PANI-NDSA. The flat region above 0.01 V indicates a charge accumulation at the interface PANI-NDSA/electrolyte which behaves like a plane capacitor with a zero band bending. The potentials of the valence and conduction band (VB and CB) are given by[58]:

$$P = 4.75 + e E_{fb} + 0.056 (\text{pH} - \text{pH}_{PZC}) + E_a \quad (5)$$

$$P_{VB} = E_{fb} + E_a - E_g \quad (6)$$

$$P_{CB} = P_{VB} - E_g \quad (7)$$

PZC (= 4.30) is the point of zero charge. The P_{CB} value (-0.75 V / 4.0 eV) is more cathodic than hydrogen evolution reaction and should lead a spontaneous hydrogen evolution under illumination. Hence, the valence band is located at (1.21 V i.e. at 5.96 eV) below vacuum.

The EIS measurements of PANI-NDSA, plotted at the open circuit potential (OCP), permit to quantify the various contributions (bulk, grains boundaries and diffusion) at the interface PANI-NDSA/electrolyte. The first semi-circle obtained in the diagram (Z_{im} versus Z_{real} , **Fig. 10. (a)**) is slightly depressed indicating a deviation from pure capacitor, $Q(i\omega)^{-k}$ is related to the phase angle φ ($= n\pi/2$), ω the angular frequency and k is the homogeneity factor ($0 < k \leq 1$). The semicircle is due to the bulk material ($R_2 = 437 \Omega \text{ cm}^2$) whose center is localized below the abscissa axis with a depletion angle and the impedance of the phase constant element (CPE₁-P). The line at low frequencies, inclined at 62.3° indicates the disparity from a pure Warburg diffusion R_w ($= 1.076 \text{ K}\Omega \text{ cm}^2$). The small shift from the origin ($\sim 42 \Omega \text{ cm}^2$) is attributed to the electrolyte resistance (R_1 , Na_2SO_4 0.1 M). The data are modeled to an electrical equivalent circuit comprising the resistance R_1 connected in series with the resistance R_w in parallel with the CPE₂-P. The EIS data are suitably adjusted to the proposed equivalent electrical circuit by using the software Zview (**Fig. 10. (a), Inset**).

The Bode representation i.e. $|Z|$ and phase angle φ as a function of \log (frequency) is illustrated in **Fig. 10. (b)**. Let's recall that for a capacitive behavior, φ approaches -90° while a tendency to 0° is reached for pure resistance. The phase φ increases up to 37° with raising the frequency in the range (10^{-2} - 10^5 Hz), confirming the circuit R_{ct} - C_{dl} where R_{ct} is the charge transfer resistance, C_{dl} the capacity of the double layer (**Fig. 10. (b)**), the two negative slopes at intermediate frequencies, indicate a semi-capacitive behavior with two CPE (1 and 2).

The current density in the $J(E)$ characteristic ($\sim 0.5 \text{ mA/ cm}^2$) under visible light insert Fig. 8. Predicts an easy electronic transfer through the PANI-NDSA/electrolyte interface. Such behavior is corroborated by the small diameter (R_2 $437 \Omega \text{ cm}^2$). Such value is desirable in the photo-catalytic H_2 formation (see below).

Photocatalysis

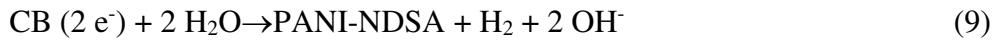
PANI-NDSA is applied for the H_2 photoproduction and the chemical stability is of high importance and must be taken into account for the long-term applications. For this purpose, we have examined the stability by storing PANI-NDSA over one week in the working solution

(pH=7) and no degradation was detected. On the contrary, in alkaline electrolyte the color turns to brown a behavior attributed to dedoping phenomenon, resulting from the neutralization of bi-polarron sites.

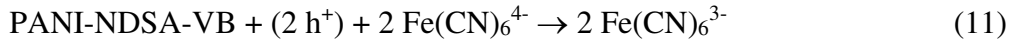
On the other hand, the water photo splitting needs an optical gap E_g greater than 2.4 eV taking into accounts the O_2^- and H_2 -over-potentials. There for oxygen cannot be released on PANI-NDSA because of, i) its narrow gap (1.96 eV) and ii) the position of the valence band, less anodic than that of O_2/H_2O level. Hence, reducing specie must be added to react with the photoholes, which should result in enhanced photocatalytic performance. In such a case, $Fe(CN)_6^{2-}$ oxidation occurs quickly enough to maintain the holes concentration low in order to preclude the photo corrosion of PANI-NDSA. Hydrogen is evolved according to the following mechanism:



Cathodic pole



Anodic pole



A good activity is obtained at pH 6.8 in presence of $Fe(CN)_6^{2-}$ which favours the separation of charge charges (reaction 11) and protect the catalyst against the photocorrosion. The volume of evolved hydrogen increases monotonically over illumination time with an average rate of $3840 \mu\text{mol h}^{-1} (\text{g catalyst})^{-1}$. The end product $Fe(CN)_6^{2-}$ competes with water for the photoelectrons (reaction 10); its redox potential ($\sim 0.12 \text{ V}$) is close to that of H_2O/O_2 level and should maintain a more or less linear behaviour. Indeed; when the reaction product, $Fe(CN)_6^{3-}$ in the present case, is not withdrawn from the electrolytic solution by a chemical or physical process, it react at the opposite pole of the crystallite leading to a decline in the photocatalytic activity. This occurs with $Fe(CN)_6^{2-}$, where the rate is high at the beginning and gradually slows down over time (**Fig. 12**). PANI-NDSA is black and absorbs over the whole solar spectrum, thus permitting the determination of the quantum efficiency (η) of photons into hydrogen:

$$\eta = 2 \times \left\{ \frac{NV}{V_m P t_{(s)}} \right\} \times 100 \quad (11)$$

Where N is the Avogadro number, V the volume of evolved H_2 , V_m the molar volume and P the incident photons (2.09×10^{19} photons s^{-1}). The factor 2 in the relation 12 enters because the H_2 molecule requires two electrons; a value of 0.34% is determined. Interestingly, the initial activity of the catalyst during the second cycle is practically restored and very weak deactivation ($< 2\%$) is observed (**Fig. 12**). The hetero-system PANI-NDSA/ZnO will be applied for the reduction of heavy metals like nickel upon visible light. The preliminary results are conclusive and the detailed study will be reported very soon.

It is instructive at this level to compare the performance of PANI-NDSA with those already reported in the literature (Table 1). One can see that our catalyst shows an activity far superior than most modified PANIs. Moreover, we worked under visible light irradiation with a catalyst dose less than 0.5 g L^{-1} .

Conclusion

PANI-NDSA is chemically stable, inexpensiveness and non-toxic. Its semiconducting properties have been studied for the first time to assess its photocatalytic hydrogen evolution upon visible irradiation. It is thermally stable up to $\sim 290 \text{ }^\circ\text{C}$ and the X-ray diffraction indicated broad peaks, characteristic of nano-morphology and a crystallite size of $\sim 7 \text{ nm}$. An optical transition at 1.96 eV , directly permitted is obtained from the diffuse reflectance. The electrical conductivity obeys to an exponential law with activation energy of 0.24 eV . The p -type behavior of PANI-NDSA is highlighted from the (capacitance⁻² – potential) plot. A flat band potential (E_{fb}) of 0.82 V_{SCE} was determined in neutral electrolyte. The contributions of the bulk and grain boundaries predominate in the electric conductivity. PANI-NDSA is successfully employed for the hydrogen formation when exposed to visible irradiation because the potential of its conduction band is more cathodic than that of H_2O/H_2 . A quantum yield of 0.34% was obtained using $Fe(CN)_6^{4-}$ as hole scavenger. The photoactivity was completely restored during the second cycle.

Acknowledgments

The authors thank Dr S. Kabouche for his assistance and fruitful discussion in electrochemistry. The Faculties of Chemistry financially supported this work.

References

1. A. Jäger-Waldau, *Energies* **12**, 769 (2019).
2. N. M. Haegel, H. Atwater, T. Barnes, C. Breyer, A. Burrell, Y.-M. Chiang, S. De Wolf, B. Dimmler, D. Feldman, and S. Glunz, *Science* (80-.). **364**, 836 (2019).
3. Ü. Ağbulut and S. Sarıdemir, *Int. J. Ambient Energy* **1** (2019).
4. S. Wu, G. Xiong, H. Yang, Y. Tian, B. Gong, H. Wan, Y. Wang, T. S. Fisher, J. Yan, and K. Cen, *Matter* **1**, 1017 (2019).
5. F. Saib, F. Özel, A. Sarılmaz, O. Mahroua, B. Bellal, and M. Trari, *Mater. Sci. Semicond. Process.* **91**, 174 (2019).
6. R. Bagtache, F. Saib, K. Abdmeziem, and M. Trari, *Int. J. Hydrogen Energy* (2019).
7. D. Hamane, O. Arous, F. Kaouah, M. Trari, H. Kerdjoudj, and Z. Bendjama, *J. Environ. Chem. Eng.* **3**, 60 (2015).
8. F. Saib, O. Arous, A. Mazari, and M. Trari, **1800245**, 1 (2019).
9. R. L. Glicksman, D. L. Markell, W. W. Buzbee, D. R. Mandelker, and D. Bodansky, *Environmental Protection: Law and Policy* (Aspen Publishers, 2019).
10. G. Rekhila, Y. Bessekhoud, and M. Trari, *Int. J. Hydrogen Energy* **40**, 12611 (2015).
11. M. Benamira, H. Lahmar, L. Messaadia, G. Rekhila, F.-Z. Akika, M. Himrane, and M. Trari, *Int. J. Hydrogen Energy* (2019).
12. M. Silakhori, M. Jafarian, M. Arjomandi, and G. J. Nathan, *J. Energy Storage* **21**, 216 (2019).
13. K. Motai and M. Miyake, (2018).
14. J. W. Ager and A. A. Lapkin, *Science* (80-.). **360**, 707 (2018).
15. J. Joy, J. Mathew, and S. C. George, *Int. J. Hydrogen Energy* **43**, 4804 (2018).
16. Z. Wang, C. Li, and K. Domen, *Chem. Soc. Rev.* **48**, 2109 (2019).
17. S. Wang, G. Liu, and L. Wang, *Chem. Rev.* **119**, 5192 (2019).
18. X. Gao, I. Di Bernardo, P. Kreider, T. Tran-Phu, X. Cai, N. Wang, Y. Zhu, M. B. Venkataraman, J. Lipton-Duffin, and A. Bayon, *ACS Catal.* **9**, 9880 (2019).
19. N. B. Goikoetxea, M. B. Gómez-Mancebo, R. Fernández-Saavedra, F. Borlaf, F. García-Pérez, J. A. Jiménez, I. Llorente, I. Rucandio, and A. J. Quejido, *Int. J. Hydrogen Energy* (2019).
20. A. Belhadi, M. Trari, C. Rabia, and O. Cherifi, (2013).
21. A. R. Marlinda, N. Yusoff, A. Pandikumar, N. M. Huang, O. Akbarzadeh, S. Sagadevan,

- Y. A. Wahab, and M. R. Johan, *Int. J. Hydrogen Energy* (2019).
22. M. Liu, C.-Y. Nam, C. T. Black, J. Kamcev, and L. Zhang, *J. Phys. Chem. C* **117**, 13396 (2013).
23. T. R. Hellstern, A. C. Nielander, P. Chakthranont, L. A. King, J. J. Willis, S. Xu, C. MacIsaac, C. Hahn, S. F. Bent, and F. B. Prinz, *ACS Appl. Nano Mater.* **2**, 6 (2019).
24. J. A. Joseph, S. B. Nair, K. A. John, S. Babu, S. Shaji, V. K. Shinoj, and R. R. Philip, *J. Appl. Electrochem.* **1** (2019).
25. X. Yuan, M. Sun, Y. Yao, X. Lin, and J. Shi, *New J. Chem.* **43**, 2665 (2019).
26. C. M. Magdalane, K. Kanimozhi, M. V Arularasu, G. Ramalingam, and K. Kaviyarasu, *Surfaces and Interfaces* 100346 (2019).
27. L. Zhang, W. Yu, C. Han, J. Guo, Q. Zhang, H. Xie, Q. Shao, Z. Sun, and Z. Guo, *J. Electrochem. Soc.* **164**, H651 (2017).
28. F. Yang, Q. Zhang, L. Zhang, M. Cao, Q. Liu, and W.-L. Dai, *Appl. Catal. B Environ.* 117901 (2019).
29. Y. Qiao, X. Meng, and Z. Zhang, *Appl. Surf. Sci.* **470**, 645 (2019).
30. A. Hernández, N. Loera, G. Pérez, and F. Blockstrand, *Energy Technol. 2019 Carbon Dioxide Manag. Other Technol.* 133 (2019).
31. I. Tseng, Y.-M. Sung, P.-Y. Chang, and C.-Y. Chen, *Polymers (Basel)*. **11**, 146 (2019).
32. F. Saib, B. Bellal, and M. Trari, *Mater. Sci. Semicond. Process.* **63**, 122 (2017).
33. F. Saib, M. Mekiri, B. Bellal, M. Chibane, and M. Trari, *Russ. J. Phys. Chem. A* **91**, 1562 (2017).
34. Y. Wang, F. Silveri, M. K. Bayazit, Q. Ruan, Y. Li, J. Xie, C. R. A. Catlow, and J. Tang, *Adv. Energy Mater.* **8**, 1801084 (2018).
35. L. Wang, D. Yan, D. W. Shaffer, X. Ye, B. H. Layne, J. J. Concepcion, M. Liu, and C.-Y. Nam, *Chem. Mater.* **30**, 324 (2018).
36. X. Yuan, D. Dragoie, P. Beaunier, D. B. Uribe, L. Ramos, M. G. Méndez-Medrano, and H. Remita, *J. Mater. Chem. A* **8**, 268 (2020).
37. P. Audebert and F. Miomandre, *Handb. Conduct. Polym.* **3**, (2019).
38. T. K. Das and S. Prusty, *Polym. Plast. Technol. Eng.* **51**, 1487 (2012).
39. L. Zhang, G. Xia, X. Li, G. Xu, B. Wang, D. Li, A. Gavriluk, J. Zhao, and Y. Li, *Synth. Met.* **248**, 88 (2019).
40. L. Bach-Toledo, B. M. Hryniewicz, L. F. Marchesi, L. H. Dall'Antonia, M. Vidotti, and F. Wolfart, *Mater. Sci. Energy Technol.* (2019).
41. M. Bhaumik, A. Maity, T. S. Mahule, and V. V Srinivasu, *Synth. Met.* **249**, 63 (2019).

42. S. Zhang, S. Chen, Y. Zhao, J. Kang, J. Chen, B. Yan, Y. Gu, F. Yang, and Y. Cao, J. Electrochem. Soc. **166**, H77 (2019).
43. M. Soleimani-Lashkenari, S. Rezaei, J. Fallah, and H. Rostami, Synth. Met. **235**, 71 (2018).
44. J. Feng, L. Ding, S. Ye, X. He, H. Xu, Y. Tong, and G. Li, Adv. Mater. **27**, 7051 (2015).
45. J.-X. Feng, S.-Y. Tong, Y.-X. Tong, and G.-R. Li, J. Am. Chem. Soc. **140**, 5118 (2018).
46. A. Shirmardi, M. A. M. Teridi, H. R. Azimi, W. J. Basirun, F. Jamali-Sheini, and R. Yousefi, Appl. Surf. Sci. **462**, 730 (2018).
47. B. Liu, X. Liu, J. Liu, C. Feng, Z. Li, C. Li, Y. Gong, L. Pan, S. Xu, and C. Q. Sun, Appl. Catal. B Environ. **226**, 234 (2018).
48. Z. Ren, X. Liu, Z. Zhuge, Y. Gong, and C. Q. Sun, Chinese J. Catal. **41**, 180 (2020).
49. Z. Zhuge, X. Liu, T. Chen, Y. Gong, C. Li, L. Niu, S. Xu, X. Xu, Z. A. Allothman, and C. Q. Sun, Chem. Eng. J. 127838 (2020).
50. B. Liu, X. Liu, L. Li, Z. Zhuge, Y. Li, C. Li, Y. Gong, L. Niu, S. Xu, and C. Q. Sun, Appl. Surf. Sci. **484**, 300 (2019).
51. X. Liu, B. Liu, L. Li, Z. Zhuge, P. Chen, C. Li, Y. Gong, L. Niu, J. Liu, and L. Lei, Appl. Catal. B Environ. **249**, 82 (2019).
52. S. K. Pillalamarri, F. D. Blum, A. T. Tokuhito, and M. F. Bertino, Chem. Mater. **17**, 5941 (2005).
53. J. E. Fischer, Q. Zhu, X. Tang, E. M. Scherr, A. G. MacDiarmid, and V. B. Cajipe, Macromolecules **27**, 5094 (1994).
54. A. Rahy and D. J. Yang, Mater. Lett. **62**, 4311 (2008).
55. Z. Zhang, Z. Wei, L. Zhang, and M. Wan, Acta Mater. **53**, 1373 (2005).
56. J. Huang and M. Wan, J. Polym. Sci. Part A Polym. Chem. **37**, 1277 (1999).
57. A. Charba, (2011).
58. F. Saib, F. Özel, A. Sarilmaz, O. Mahroua, B. Bellal, and M. Trari, Mater. Sci. Semicond. Process. **91**, 174 (2019).
59. K. He, M. Li, and L. Guo, Int. J. Hydrogen Energy **37**, 755 (2012).
60. C. Wang, L. Wang, J. Jin, J. Liu, Y. Li, M. Wu, L. Chen, B. Wang, X. Yang, and B.-L. Su, Appl. Catal. B Environ. **188**, 351 (2016).
61. C.-J. Chang and K.-W. Chu, Int. J. Hydrogen Energy **41**, 21764 (2016).
62. S. Zhang, Q. Chen, D. Jing, Y. Wang, and L. Guo, Int. J. Hydrogen Energy **37**, 791 (2012).

Figures

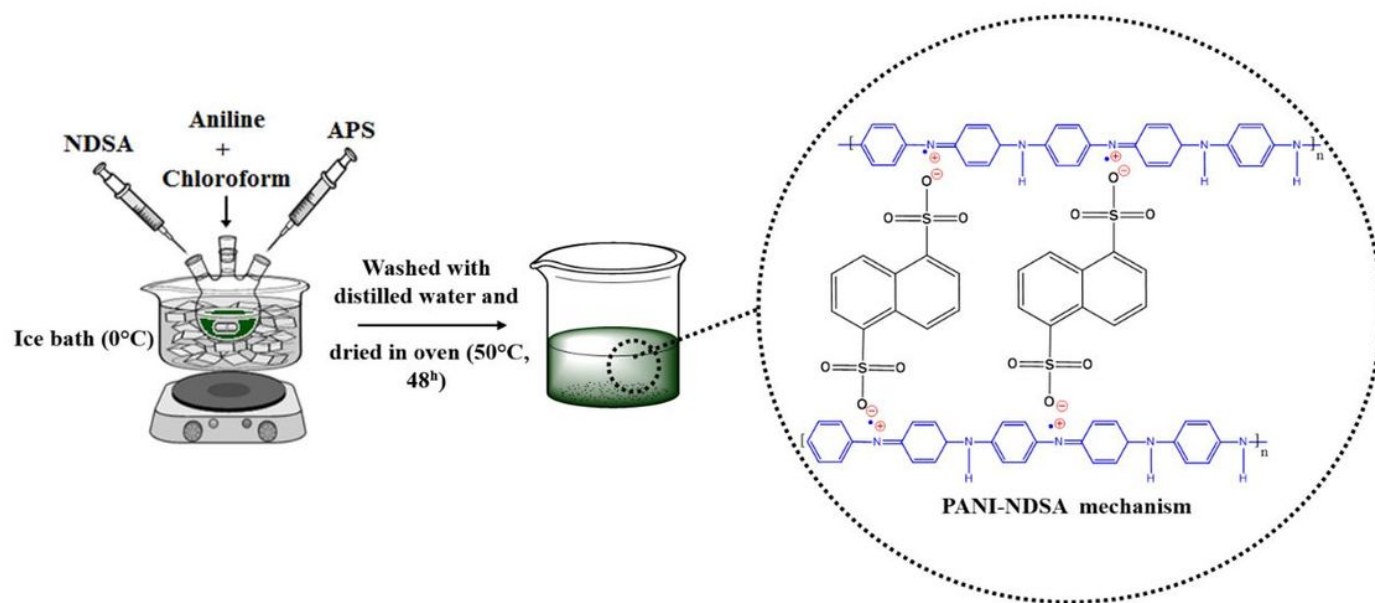


Figure 1

Synthesis process of the reactions during the formation of PANI-NDSA.

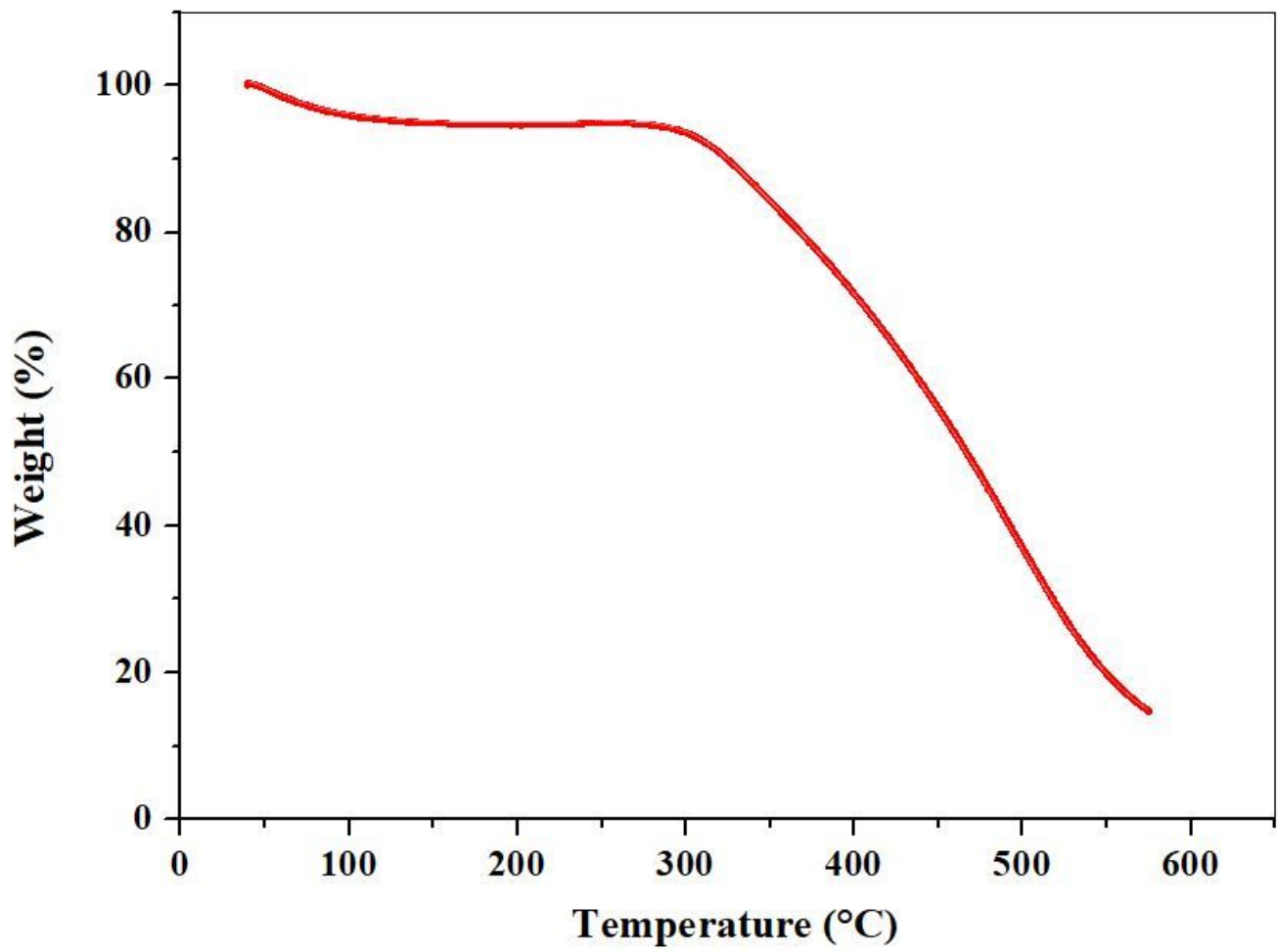


Figure 2

The TG plots of the PANI-NDSA.

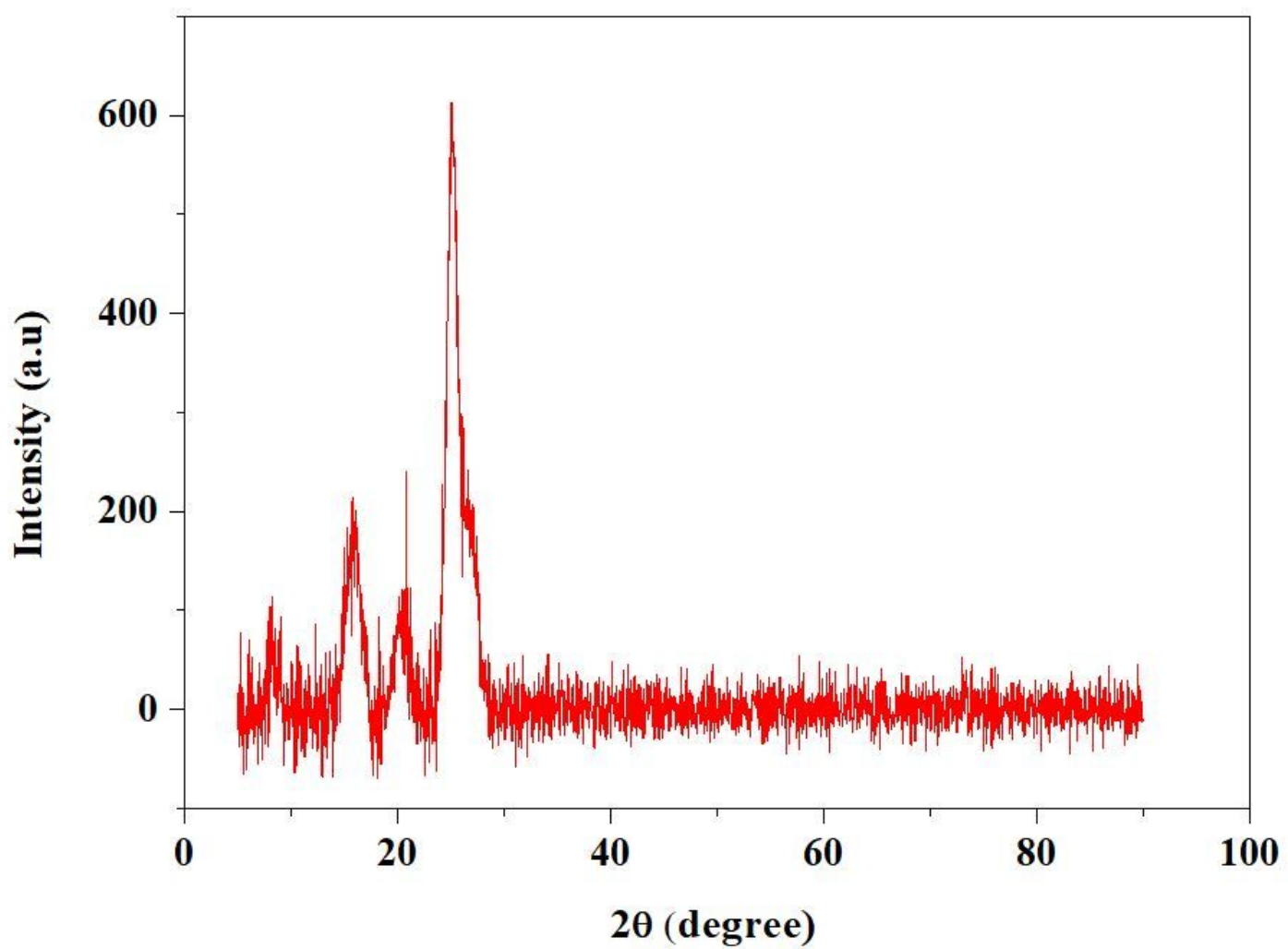


Figure 3

The X-ray diffraction pattern of PANI-NDSA

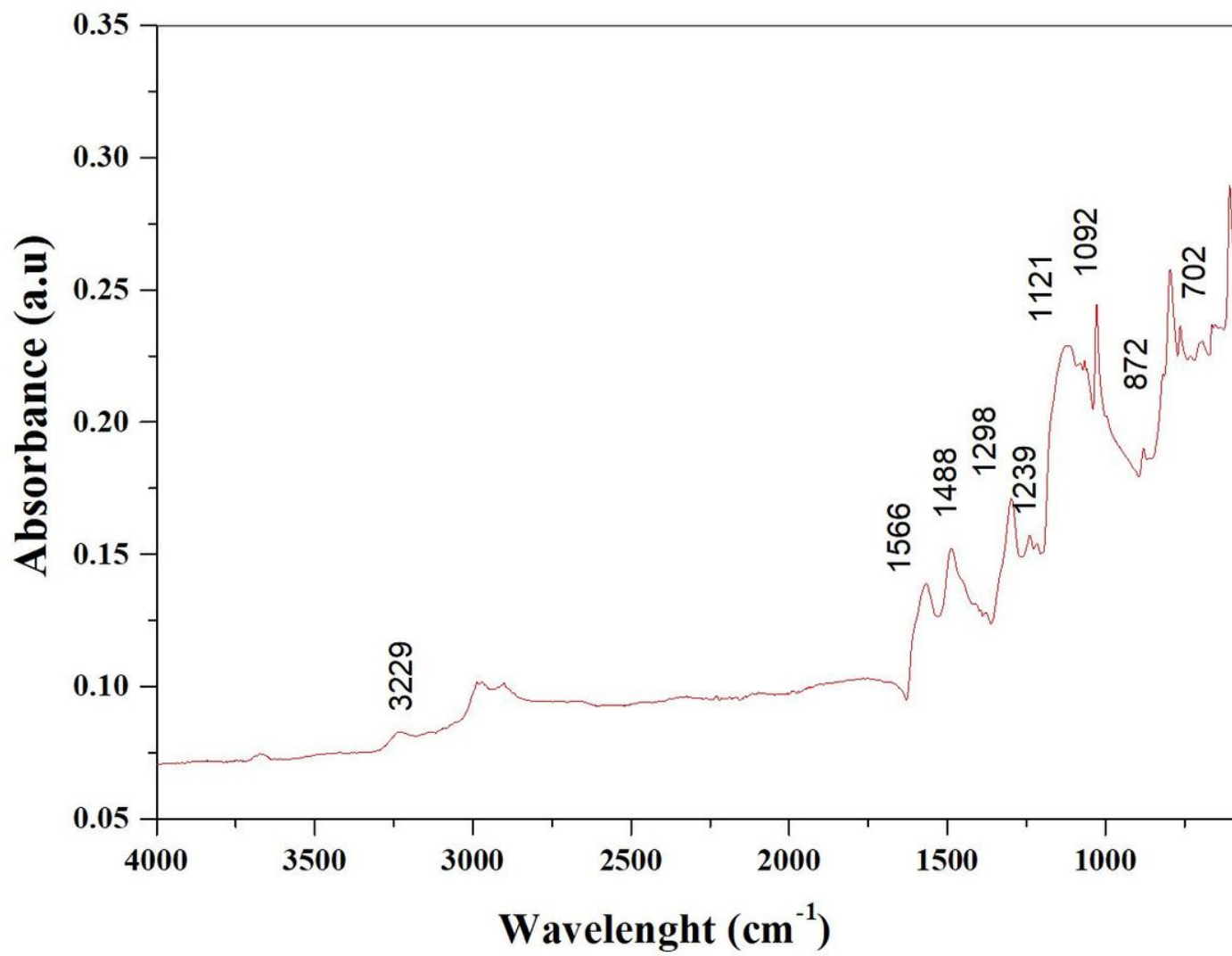


Figure 4

The FTIR spectrum of PANI-NDSA

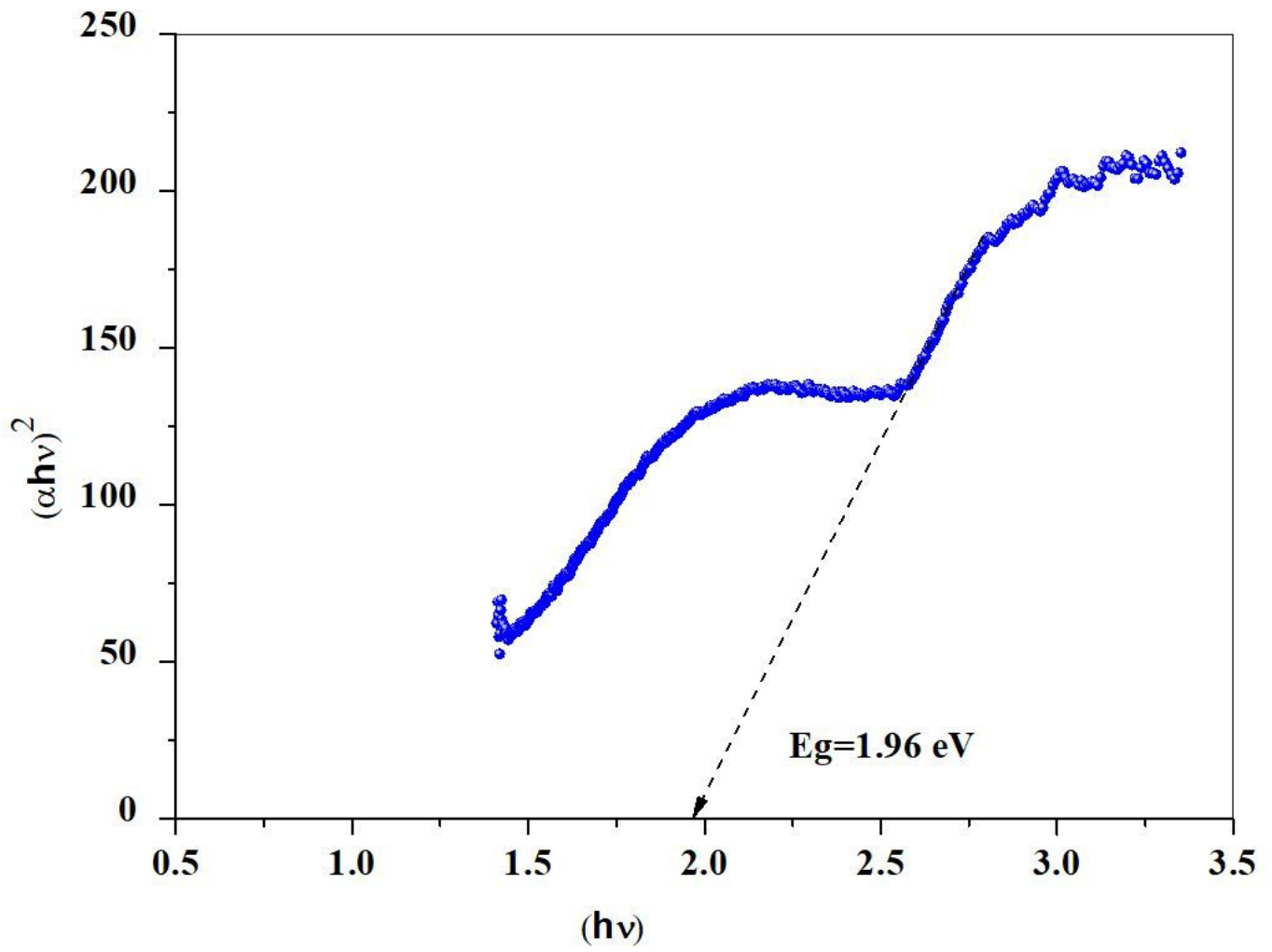


Figure 5

The direct optical transition of PANI-NDSA

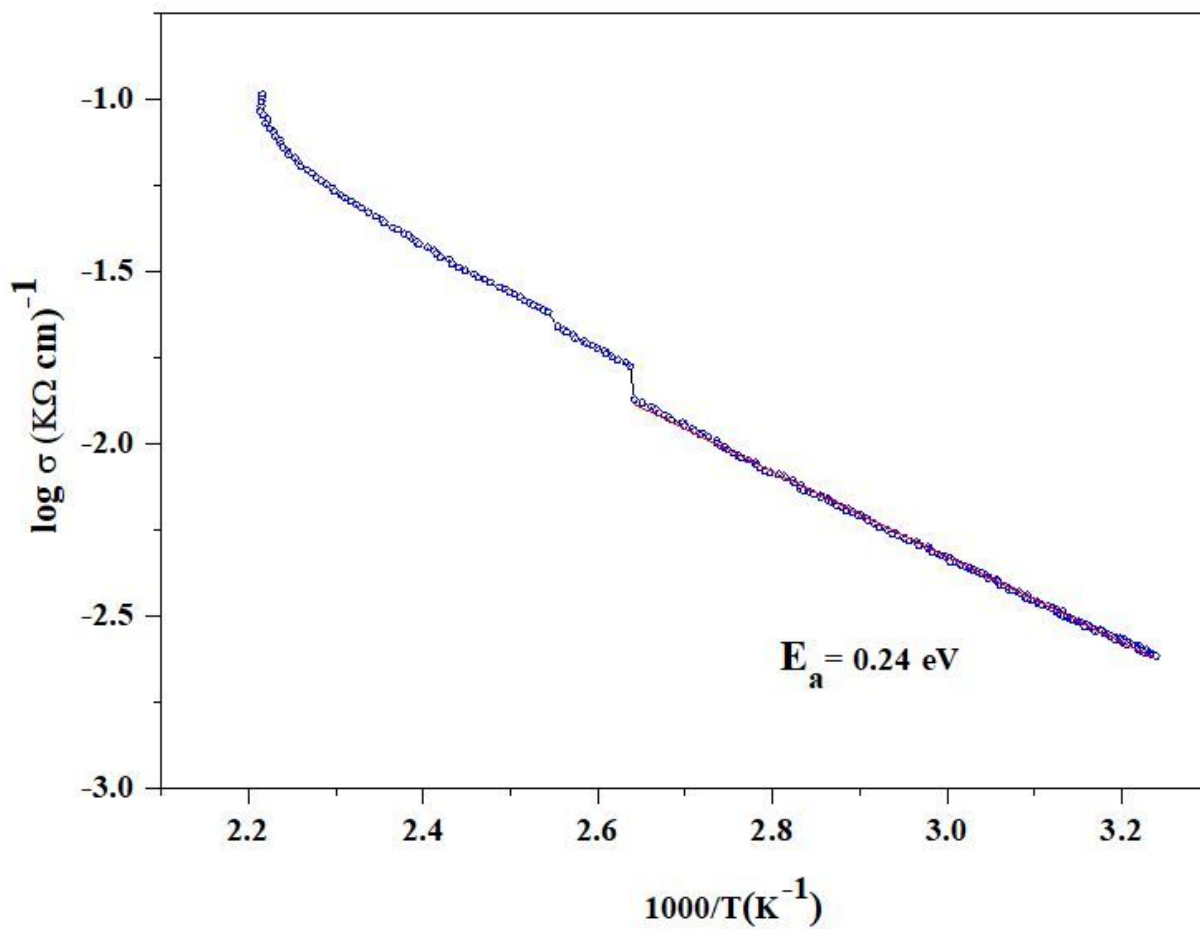


Figure 6

The thermal variation of the electrical conductivity of PANI-NDSA

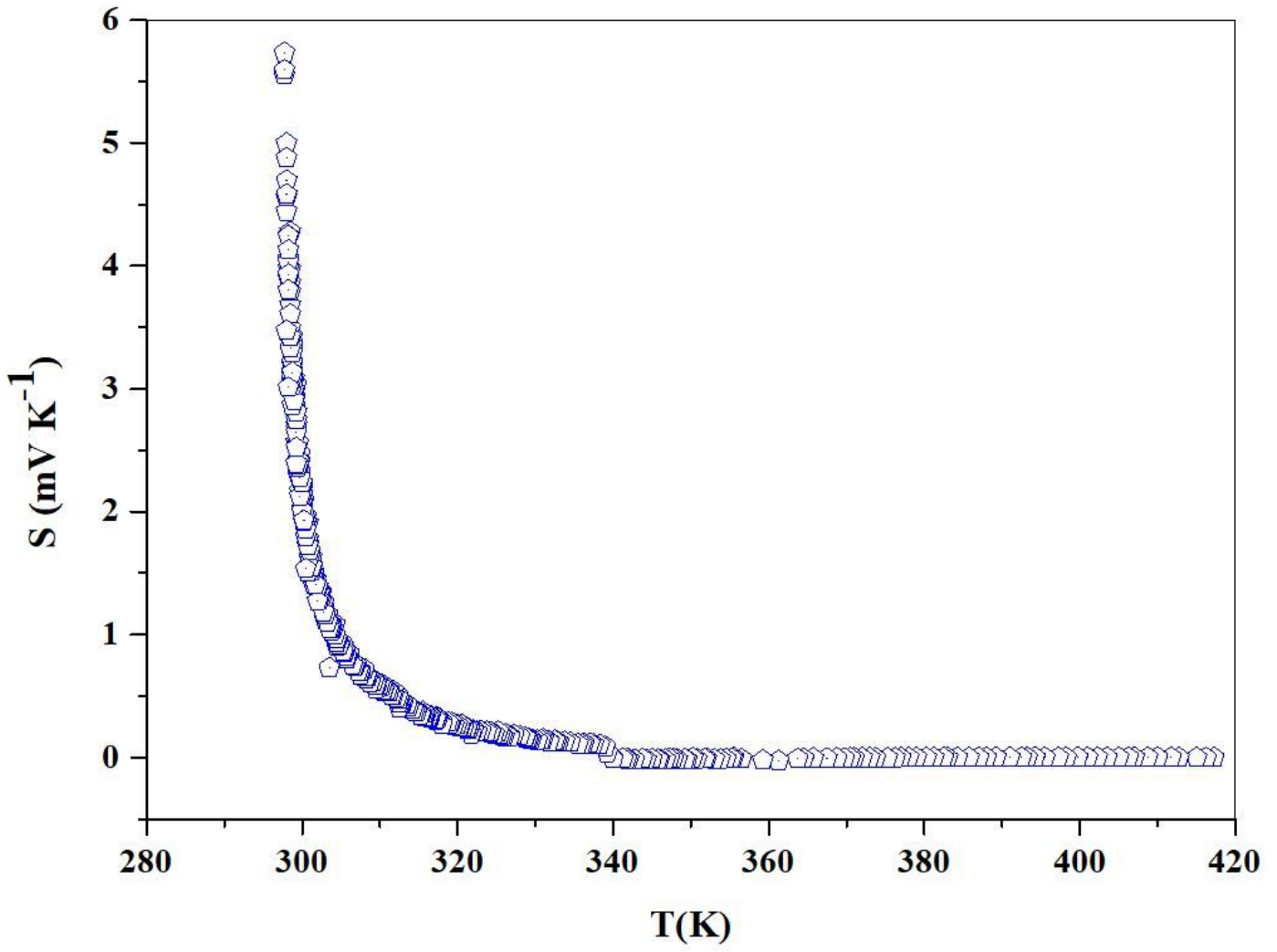


Figure 7

The thermal variation of the thermopower (S) PANI-NDSA

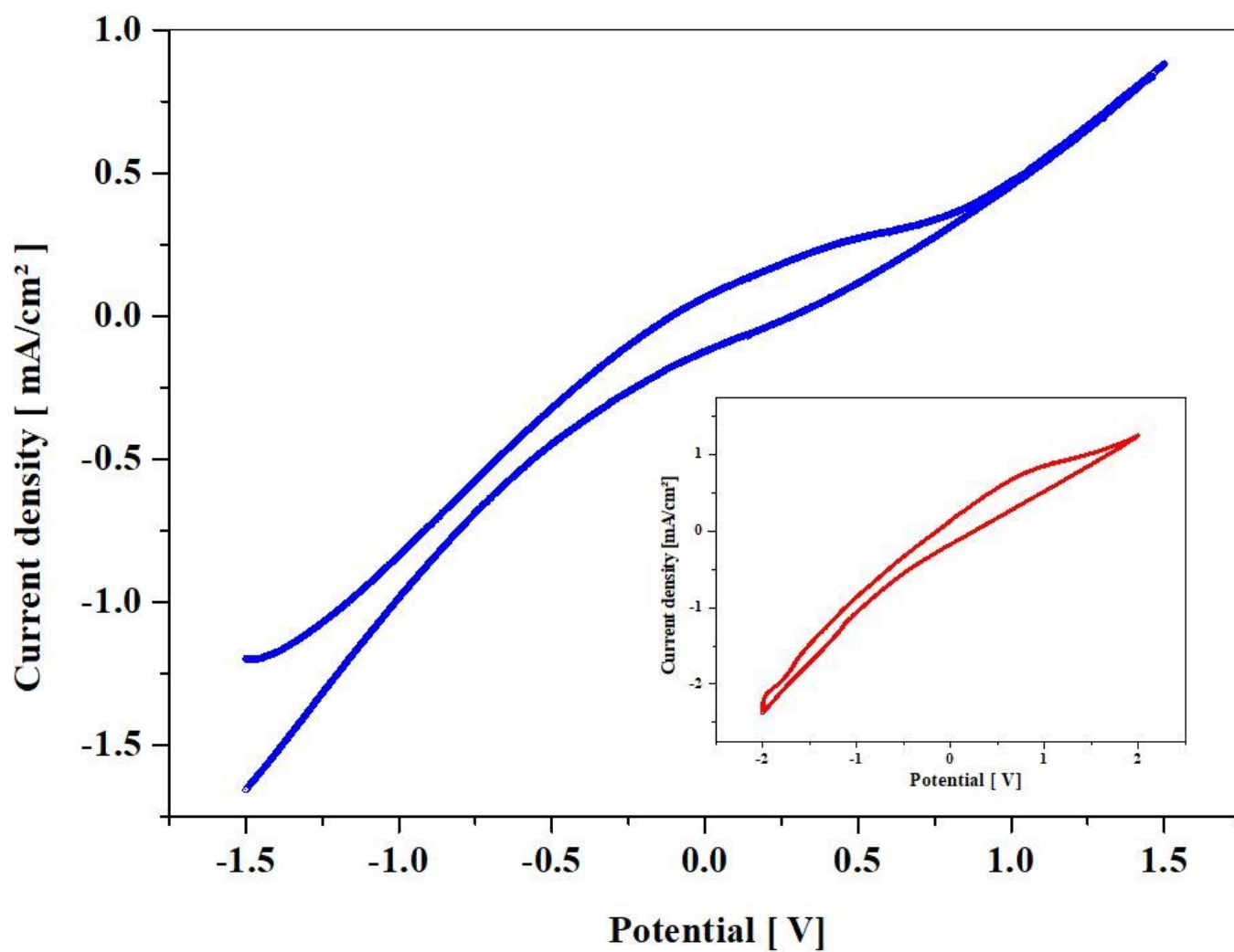


Figure 8

The dark cyclic voltammetry of PANI-NDSA in Na₂SO₄ solution (0.1 M, pH ~ 7). Inset the cyclic voltammetry under visible light

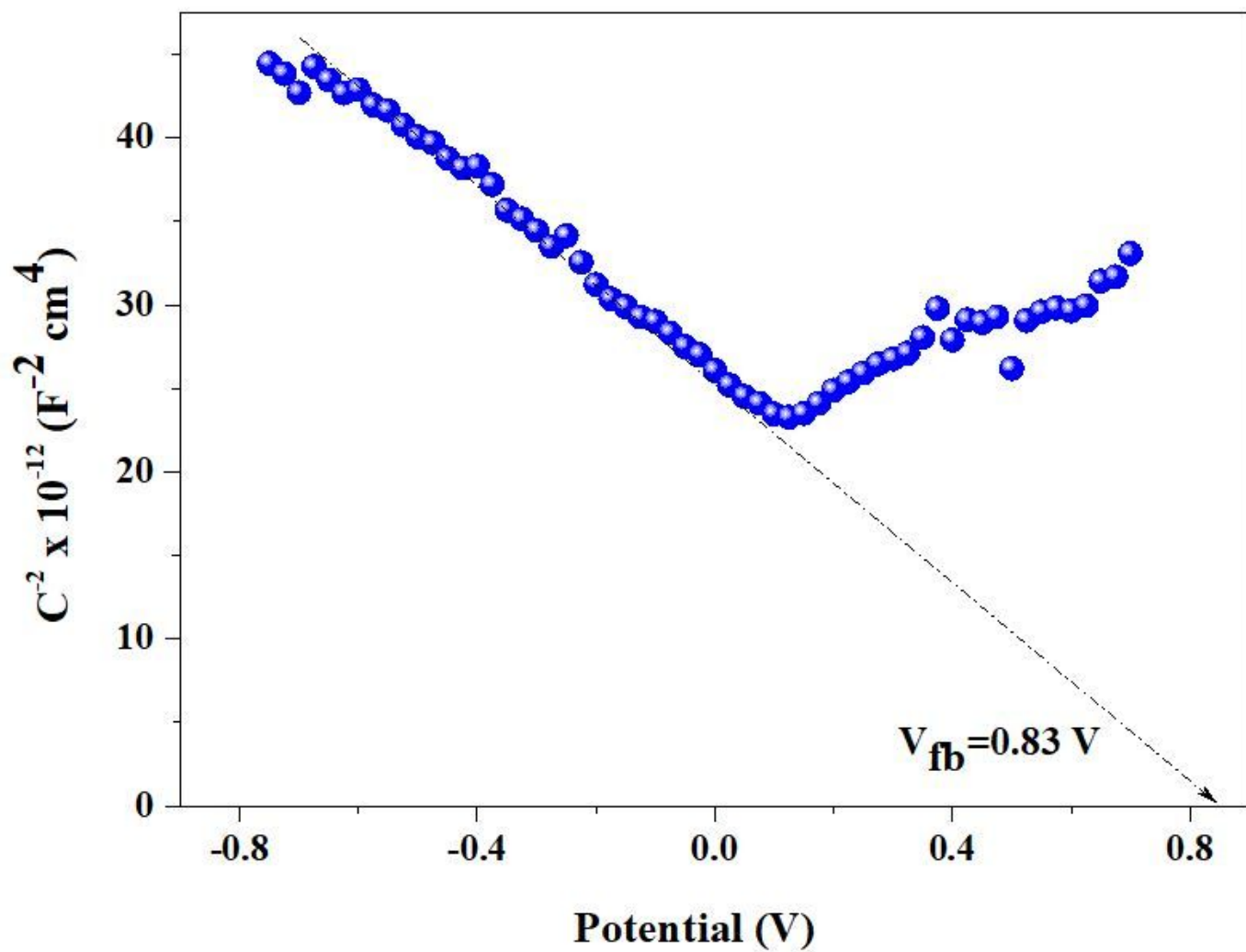


Figure 9

The Mott-Schottky characteristic of PANI-NDSA in Na₂SO₄ solution (pH ~ 7).

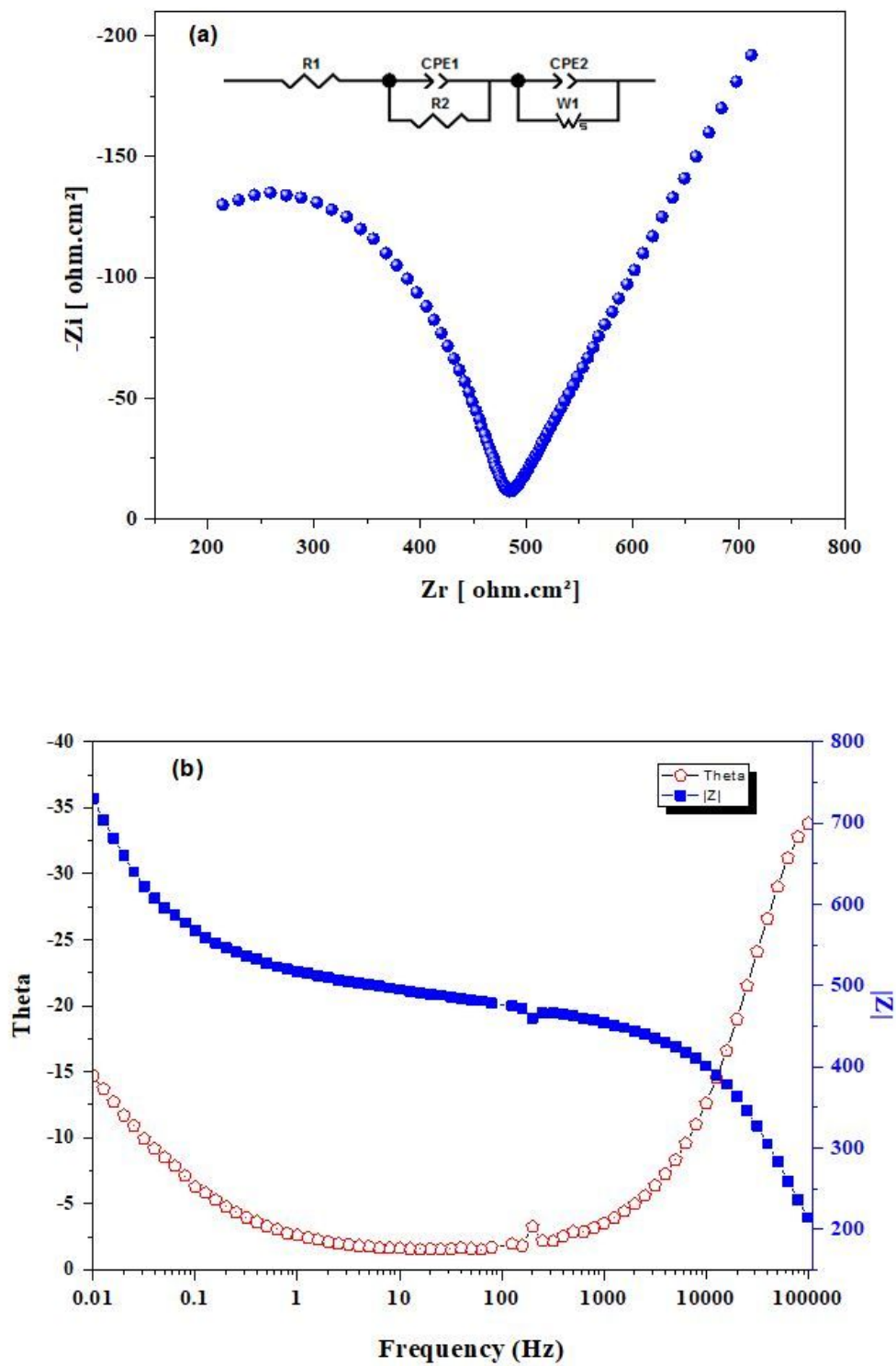


Figure 10

(a) The Nyquist representation of PANI-NDSA in Na₂SO₄ solution (pH ~ 7). Inset: the equivalent electrical circuit; (b) the Bode representation.

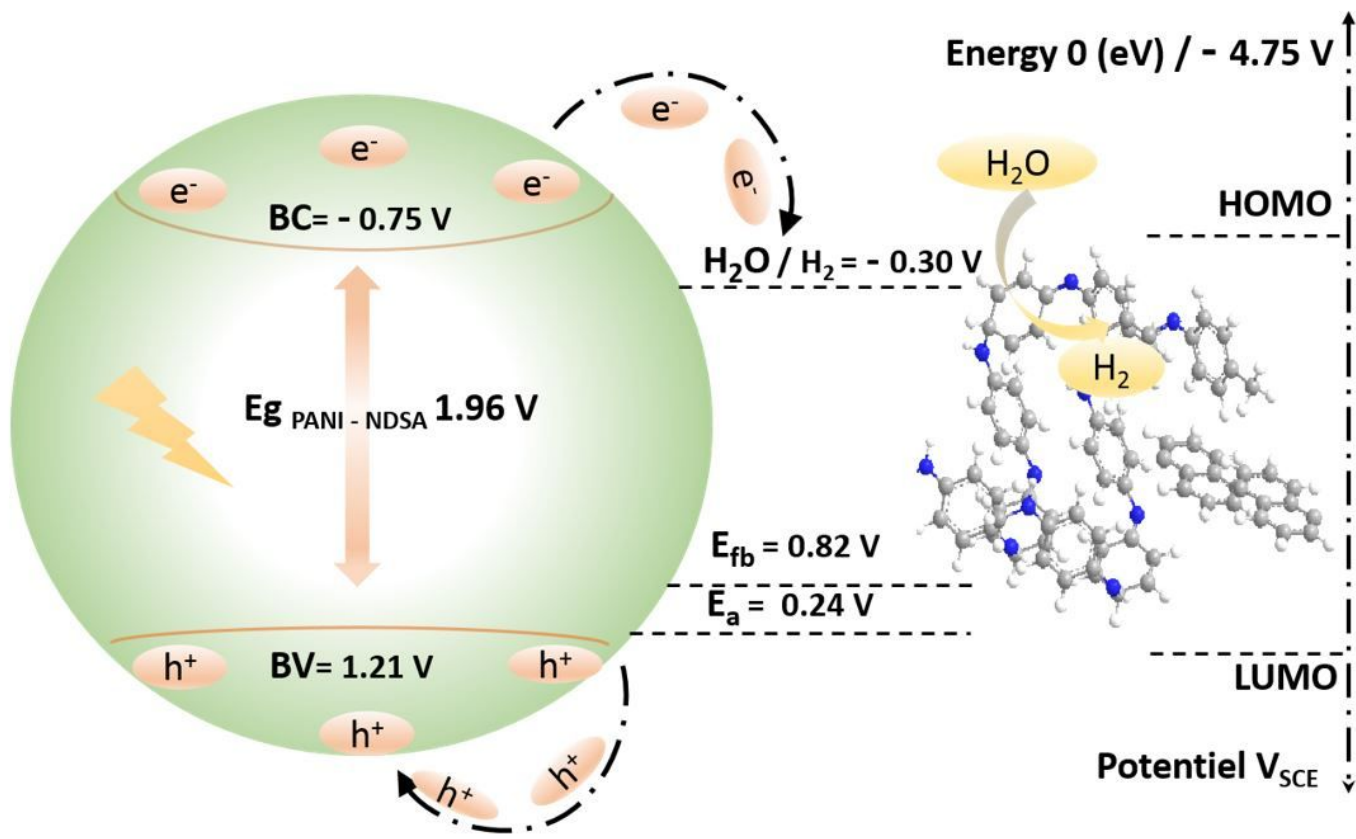


Figure 11

The energy diagram of the junction PANI-NDSA/ Na_2SO_4 solution.

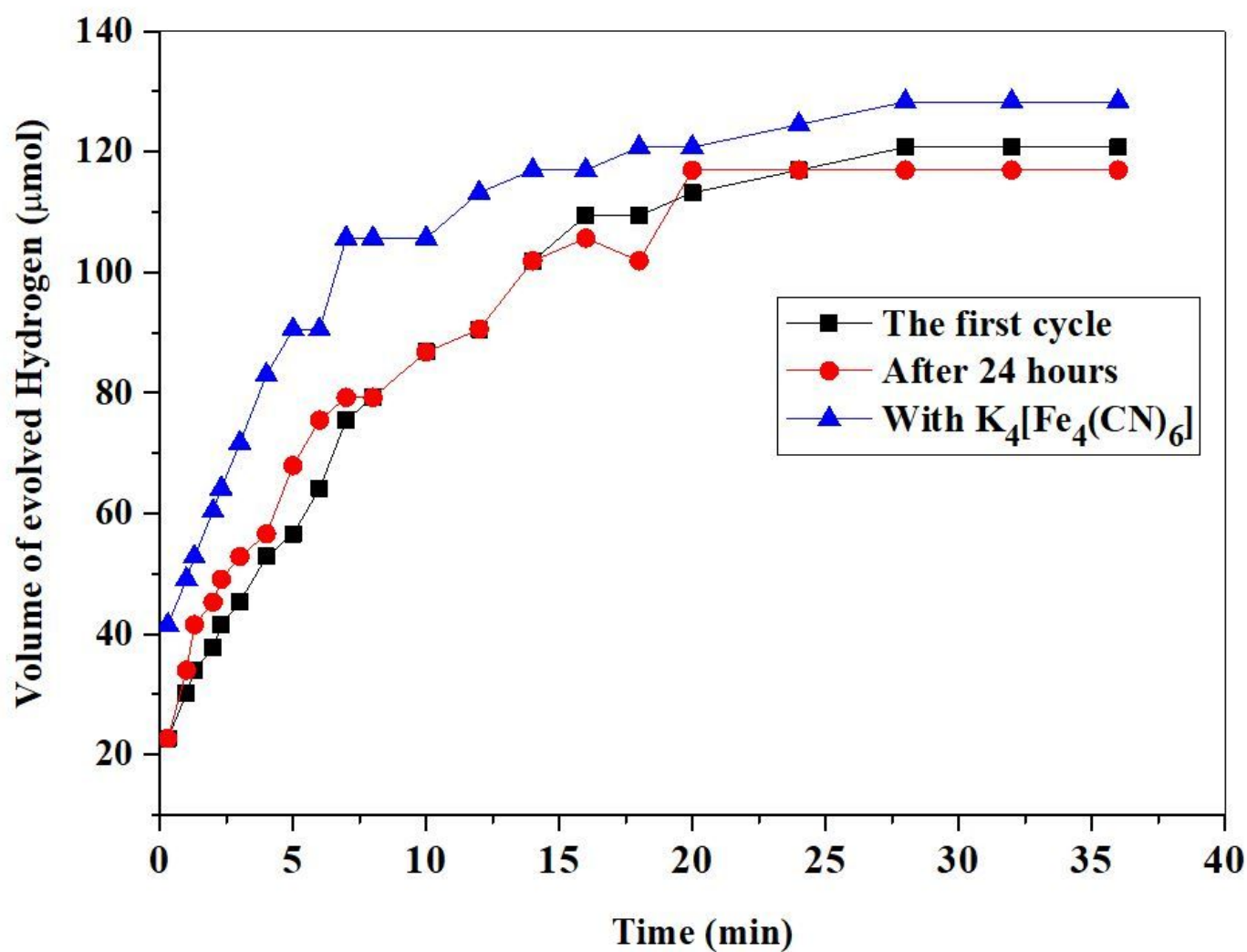


Figure 12

The volume of evolved hydrogen on PANI-NDSA in Na_2SO_4 solution (pH ~ 7).

Supplementary Files

This is a list of supplementary files associated with this preprint. Click to download.

- [scheme1.jpg](#)